PCCP

ROYAL SOCIETY OF CHEMISTRY

PAPER

View Article Online
View Journal



Cite this: DOI: 10.1039/d6cp00343e

# Electron–electrophile coupled dinitrogen reduction in a cerium–*meta*-tetraphenolate system: a computational study

Shahbaz Ahmad, [a] Polly L. Arnold *[b] and Nikolas Kaltsoyannis *[a]

Received 30th January 2026,
Accepted 2nd March 2026

DOI: 10.1039/d6cp00343e

rsc.li/pccp

The use of lanthanide complexes for catalytic dinitrogen reduction is a new development in homogeneous catalysis. Density functional theory calculations on our recently reported cerium phenolate catalyst $[K_2Ce_2(sol)_4(mTP)_2]$ (*m*TP = {$(OC_6H_2$-2-$^t$Bu-4-Me$)_2CH\}_2$-1,3-$C_6H_4$; sol = $OMe_2$ here; THF in the experiment) have been undertaken to elucidate the reduction, activation and silylation steps at the bound dinitrogen molecule, in the presence of the reductant, potassium metal ($K^0$) and the electrophile $Me_3SiCl$ (TMSCl). Out of the total of six electron reductions required to cleave the $N_2$, the first two-electron reduction step was found to be highly disfavoured unless potassium cations ($K^+$) are included, upon which the step is rendered strongly exergonic; N–Si bond formation at the two-electron stage is predicted to be unfavourable. The three-electron-reduced $N_2$-adduct is found to be at the reductive activation limit in the absence of added electrophiles, which can form N-element bonds and lower the overall charge. Added electron density beyond three-electron reduction no longer localises on $N_2$, preventing formal $N_2^{4-}$ formation. A pathway in which both $K^0$ and $Me_3SiCl$ work in concert was modelled, and six sequential reduction–silylation steps were calculated, showing how the N–N bond is cleaved after the third reduction, eventually releasing two equivalents of $N(SiMe_3)_3$, and regenerating the starting complex with the highest barrier of any step being 22 kcal mol$^{-1}$. We establish alkali metal coordination and coupled electron–electrophile transfer as key factors in the design of rare-earth-mediated dinitrogen functionalisation.



## Introduction

The catalytic conversion and fixation of atmospheric dinitrogen ($N_2$) into value-added organonitrogen compounds (the nitrogen reduction reaction, N2RR; *i.e.*, the net reduction of $N_2$ to ammonia and/or organonitrogen products) remain among the foremost challenges in contemporary chemistry,[1] primarily due to the exceptional thermodynamic stability and kinetic inertness of the N≡N triple bond (bond dissociation energy ≈ 226 kcal mol$^{-1}$).[2–4] Although the industrial Haber–Bosch process continues to dominate large-scale ammonia synthesis, there are opportunities for small-scale, low-energy N2RR processes to provide energy justice to remote communities.[1,5–7] Consequently, the development of alternative strategies for $N_2$ activation and functionalisation under milder, more sustainable conditions is being pursued with growing intensity.[8–17] Molecular systems capable of mediating the reductive functionalisation of $N_2$ through multi-electron, multi-proton transformations have attracted considerable attention.[18–23] A key approach is ligand design that stabilises reduced metal centres while promoting $N_2$ binding, activation, and subsequent functionalisation.[23–25] Lanthanides are difficult to reduce; accordingly, f-block systems typically deliver electrons from an external reductant to bound $N_2$, often with alkali-metal assistance and concurrent electrophile capture, and have only recently emerged as promising candidates for N2RR.[8,9,15,26]

Among f-block elements, Sm(II) binding of $N_2$ has long been known,[27] and both Sm and Ce have now also been reported to catalyse $N_2$ functionalisation.[9,28] In the d block, Mo, Ti, and Fe systems are well developed for end-on/side-on $N_2$ binding and stepwise proton-coupled electron transfer.[9,12,29–31] We showed that strongly electron-donating tetraphenolate scaffolds stabilise dinuclear f-element $N_2$ adducts and promote multi-electron delivery; related multinucleating phenolates also support early d-metal N2RR, including Ti systems selective for secondary silylamines and the first Zr catalysts.[9] We also showed that the *m*TP ligand's benzylic CH group can be deprotonated by the bound, reduced $N_2$, enabling the first catalysts for selective conversion of $N_2$ to secondary silylamines.[8]

[a] *Department of Chemistry, University of Manchester, Oxford Road, Manchester M13 9PL, UK. E-mail: nikolas.kaltsoyannis@manchester.ac.uk*
[b] *University of California, Berkeley and Lawrence Berkeley National Laboratory, Berkeley, CA 94720, USA. E-mail: pla@berkeley.edu*

$$N_2 + 6K + 6SiMe_3Cl \xrightarrow{[K_2Ce_2(sol)_4(mTP)_2]} 6(SiMe_3)_3N + 6KCl$$

Scheme 1 Overall $N_2$-to-$N(SiMe_3)_3$ conversion with K/TMSCl: experimental stoichiometry[9] and computed Ce–*m*TP electron–electrophile-coupled mechanism.

Ce-based homogeneous N2RR remains rare and mechanistically underexplored.[32] Ce is the most abundant rare earth element, and is exceedingly difficult to reduce, so to achieve $N_2$ reduction, $Ce^{III}$ complexes require a co-reductant.[9,28,33,34] Cerium's ability to stabilise high coordination numbers and to adopt variable geometries renders it an attractive candidate for the design of complexes capable of facilitating multi-electron, multi-proton $N_2$ activation.[35–38]

Here we describe a comprehensive computational study of the mechanism of N2RR catalysed by the bimetallic Ce(III) complex **1**, $[K_2Ce_2(Me_2O)_2(mTP)_2]$ (*m*TP = *meta*-tetraphenolate), designed to elucidate the capabilities and limitations of multi-electron transfer processes within this f-block framework. The overall experimental $N_2$-to-$N(SiMe_3)_3$ stoichiometry with K/TMSCl, together with the computed Ce–*m*TP electron–electrophile-coupled mechanism, is summarised in Scheme 1. Particular attention has been given to the structural, thermodynamic, and electronic features relevant to $N_2$ binding, reduction, and subsequent functionalisation. The influence of alkali metal cations on the energetics of $N_2$ activation has been considered in detail due to the known role of different electropositive countercations in stabilising reduced $N_2$ intermediates in a variety of d-block systems, as well as in the *m*TP complexes.[39–42] More broadly, alkali-metal cations (especially $K^+$) are increasingly recognised as active promoters in molecular $N_2$ chemistry, where they can tune reduction potentials and stabilise highly reduced $N_2$-derived ligands, and in some cases influence whether N–N bond scission is accessible. These effects have been demonstrated across diverse platforms, including iron systems (alkali-metal-dependent N–N cleavage outcomes),[43,44] cobalt–dinitrogen complexes (substantially weakened N–N bonds in the presence of alkali countercations),[44] and actinide chemistry where second-sphere alkali binding can modulate $N_2$ binding and cleavage thermochemistry.[45]

## Results and discussion

All calculations have been performed using density functional theory (DFT), with full methodological details provided in the Computational Methodology section. The reduction reactions were considered both in the absence and presence of potassium metal, the former representing an electrochemical reaction and the latter the experimentally observed potassium-metal reduction reaction. This generates $K^+$ countercations which can remain inner- or outer- sphere, often providing stabilisation to intermediates. For clarity, complexes considered without explicit $K^+$ countercations are denoted $\mathbf{A}^{2-}$, $[\mathbf{A}\text{–}\mathbf{N_2}]^{4-}$, $[\mathbf{A}\text{–}\mathbf{N_2}]^{6-}$ (with $\mathbf{A}^{2-}$ = $[Ce_2(mTP)_2]^{2-}$), while those with explicit $K^+$ are denoted **1**, $[\mathbf{1}\text{–}\mathbf{N_2}]^{2-}$, $[\mathbf{1}\text{–}\mathbf{N_2}]^{4-}$ (with **1** = $[K_2Ce_2(OMe_2)_4(mTP)_2]$).

### Evaluation of electrochemical reduction feasibility

The feasibility of accessing reduced $N_2$ adducts was investigated, aiming to determine the extent of electron uptake achievable prior to any functionalisation events. In the experiment, a THF solution of the precatalyst **1** was always treated with an excess of K metal to initiate the $N_2$ reduction reaction by forming a reduced $N_2$-containing adduct that was not structurally characterized. Computationally, in the absence of alkali metal cations, two-electron reduction of the bridging $N_2$ ligand was computed to have a Gibbs energy change ($\Delta G_1$) of −50.4 kcal mol$^{-1}$, corresponding to a reduction potential of −2.89 V *versus* the standard hydrogen electrode (−3.1 V *vs.* $Fc/Fc^+$, assuming the value in THF is the same as in MeCN). Despite the process being exergonic, this potential is inaccessible using standard reductants, rendering the process electrochemically infeasible. Subsequent two-electron reduction was even more unfavourable, requiring an energy input of +26.3 kcal mol$^{-1}$ ($\Delta G_2$), thus rendering the formation of an $N_2^{4-}$ species implausible (Scheme 2).

Given the established stabilising role of alkali metal cations in promoting multi-electron reductions of small molecules,[39,40] two potassium cations ($K^+$) were introduced into the model. This modification significantly stabilised the reduced species, lowering $\Delta G_3$ for the two-electron reduction to −125.7 kcal mol$^{-1}$. Further two-electron reduction was computed to be exergonic ($\Delta G_4$ = −13.7 kcal mol$^{-1}$); however, the associated potential of −4.48 V remains too negative for standard reductants (Scheme 3). Structural comparisons of the optimised geometries revealed notable changes in cerium–nitrogen and nitrogen–nitrogen distances upon $K^+$ incorporation, suggesting cation-induced stabilisation (see Sections S1–S3 (Fig. S1.1 and S2.1–S2.3) for details of this, and other aspects of this paragraph). To evaluate the extent of reduction achievable at the $N_2$ unit—*i.e.* $N_2^{2-}$, $N_2^{3-}$, or $N_2^{4-}$—four-electron reductions were performed both

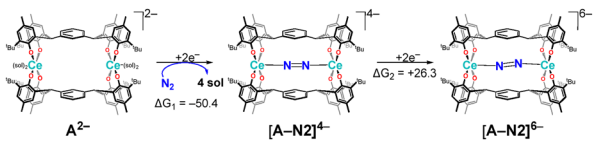


Scheme 2 Gibbs energies (kcal mol$^{-1}$) for sequential addition of between 1 and 6 electrons to $\mathbf{A}^{2-}$ with the bridging $N_2$ ligand in the absence of alkali metal cations, calculated at the PBE0-D3BJ/BS2/SMD//PBE0-D3BJ/BS1 level of theory. "sol" denotes solvent molecule and is used in subsequent schemes.

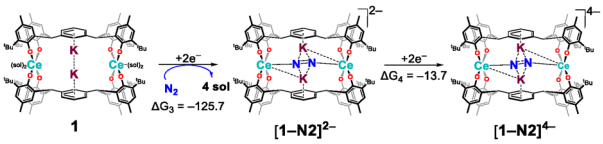


Scheme 3 Gibbs energies (kcal mol$^{-1}$) for sequential reductions of the bridging $N_2$ ligand in the presence of two explicit $K^+$ cations, calculated at the PBE0-D3BJ/BS2/SMD//PBE0-D3BJ/BS1 level of theory. Weak interactions between $K^+$ and nearby atoms are indicated by dotted lines.

with and without $K^+$ cations. Gibbs energy calculations identified the quintet spin state of the four-electron-reduced complex as more stable than the triplet in both scenarios (see Section S3 of the SI). Detailed molecular orbital and spin density analyses unequivocally demonstrated that formation of a genuine $N_2^{4-}$ species was not attained in either case. In the absence of $K^+$ cations, the additional electron density was primarily localised on the cerium centres and the ligand framework, with negligible delocalisation onto the $N_2$ unit. Upon inclusion of two $K^+$ cations, the extra electrons were distributed over the cerium centres and $K^+$ cations, meaning that full reduction of the $N_2$ moiety is not achieved. Complete reduction to $N_2^{4-}$ is therefore electronically inaccessible under these conditions. This is in agreement with experimental observations; only products of two electron-$N_2$-reduction could be isolated and spectroscopically observed.

### Evaluation of $K^0$ as a chemical reductant

Given the established use of elemental potassium in driving multi-electron reductions in f-block systems, its efficacy as a reductant was here investigated through stepwise electron transfer to the bimetallic $[K_2Ce_2(OMe_2)_2(mTP)_2]$ complex **1** following $N_2$ uptake. Gibbs energy calculations demonstrated that the first two-electron additions were strongly exergonic ($\Delta G_{1-2} = -94.6$ kcal mol$^{-1}$), and a third remained favourable ($\Delta G_{2-3} = -20.7$ kcal mol$^{-1}$), indicating the thermodynamic feasibility of up to three-electron delivery using $K^0$ (Scheme 4). These findings are in line with our experimental observations for lanthanide- and actinide-based N2RR catalysts; products of reduction were unstable in the absence of potassium cations.[8,9]

Following the two-electron reduction, Intermediate **2**, $[K_2K'_2(OMe_2)_4\{Ce_2(mTP)_2(\mu\text{-}\eta^1\text{:}\eta^1\text{-}N_2)\}]$, was optimised in both triplet and quintet spin states, with the quintet state favoured by 9.1 kcal mol$^{-1}$. This state has Ce–N distances of 2.38 Å and an elongated N–N bond length of 1.24 Å (Fig. 1), compared with that of 1.10 Å in free $N_2$, and consistent with partial population of the $N_2$ $\pi^*$ orbital and moderate activation of the N–N bond. Consistent with this assignment, the computed N–N stretching frequency for Intermediate **2** is 1651 cm$^{-1}$, indicative of substantial weakening relative to free $N_2$. To better understand the electronic distribution, CM5 charge and spin density analyses were conducted. CM5 (Charge Model 5) is a population analysis method derived from Hirshfeld partitioning and parametrised to reproduce condensed-phase dipoles and electrostatics[46] more reliably than older schemes like Mulliken[47] or Löwdin[48] charges. In Intermediate **2**, the two nitrogen atoms each carry CM5 charges of −0.60 e, yielding a total $N_2$ charge of −1.20 e

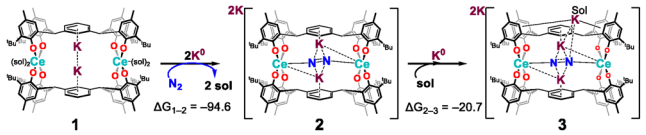


Scheme 4 Gibbs energies (kcal mol$^{-1}$) for stepwise electron transfer using $K^0$, calculated at the PBE0-D3BJ/BS2/SMD//PBE0-D3BJ/BS1 level of theory.

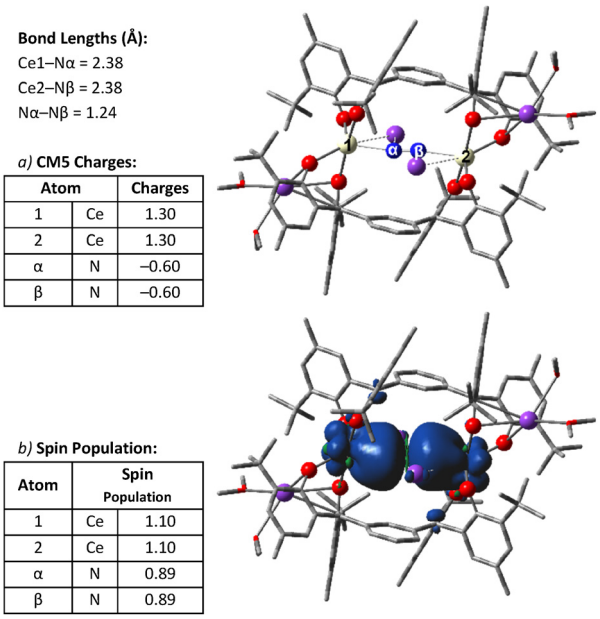


*a)* **CM5 Charges:**

| Atom | | Charges |
|---|---|---|
| 1 | Ce | 1.30 |
| 2 | Ce | 1.30 |
| α | N | −0.60 |
| β | N | −0.60 |

*b)* **Spin Population:**

| Atom | | Spin Population |
|---|---|---|
| 1 | Ce | 1.10 |
| 2 | Ce | 1.10 |
| α | N | 0.89 |
| β | N | 0.89 |

Fig. 1 Geometry of Intermediate **2** in the quintet spin state (atom colour coding: Ce = yellow, K = purple, N = blue, O = red, C = grey), optimised at the PBE0-D3BJ/BS1 level, with (a) CM5 charges and (b) spin density distribution, calculated at the PBE0-D3BJ/BS2/SMD//PBE0-D3BJ/BS1 level of theory. Isosurfaces are plotted at an isovalue of 0.0009, illustrating delocalised spin density across both Ce centres and the bridging $N_2$ ligand, with blue representing excess α spin density and green representing excess β spin density. Numerical spin populations are listed for selected atoms, indicating partial reduction of the metal centres and activation of the $N_2$ unit. Nα and Nβ denote the two nitrogen atoms coordinated to $Ce_1$ and $Ce_2$, respectively. Hydrogen atoms are omitted for clarity.

(Fig. 1a). This indicates partial reduction, *i.e.* an electronic state between $N_2^{3-}$ and $N_2^{2-}$, in line with previous observations of partially reduced $N_2$ species in f-block complexes.[8,41] Spin-density analysis (Fig. 1b), however, yields an electronic description closer to integral than shown by the CM5 charges, with each nitrogen atom bearing approximately 0.89 unpaired electrons, and with spin populations of 1.10 $e^-$ localised on each cerium centre. These values are consistent with $4f^1$ Ce(III) cerium centres, and the $N_2$ unit is close to doubly reduced.

Upon incorporation of a third electron, Intermediate **3**, $[K_2K'_2(OMe_2)_4K''(OMe_2)\{Ce_2(mTP)_2(\mu\text{-}\eta^1\text{:}\eta^1\text{-}N_2)\}]$, was calculated in both the doublet and quartet spin states, with the latter found to be more stable by 1.3 kcal mol$^{-1}$. The optimised geometry exhibits Ce–N bond lengths of 2.26 and 2.28 Å and a notably elongated N–N bond of 1.31 Å (Fig. 2), consistent with increased occupation of the $\pi^*$ manifold and further activation of the $N_2$ ligand. In line with the additional reduction, the N–N stretching frequency decreases to 1305 cm$^{-1}$ in Intermediate **3**. In the experimental system, a similarly reduced $Ln_2N_2$ adduct was measured in solution; the treatment of a THF solution of the Sm analogue of **1** with an excess of K metal under $N_2$ afforded a solution containing the pentaanionic ligand complex $[K_8(THF)_n\{Sm_2(mTP^-)_2(\mu\text{-}\eta^1\text{:}\eta^1\text{-}N_2)\}]$ with a band in the Raman spectrum at 1337 cm$^{-1}$ ($mTP^-$ {$(OC_6H_2\text{-}2\text{-}^t\text{Bu-}4\text{-Me})_2C$}{$(OC_6H_2\text{-}2\text{-}^t\text{Bu-}4\text{-Me})_2CH$}-1,3-$C_6H_4$). CM5 charge analysis yields values of

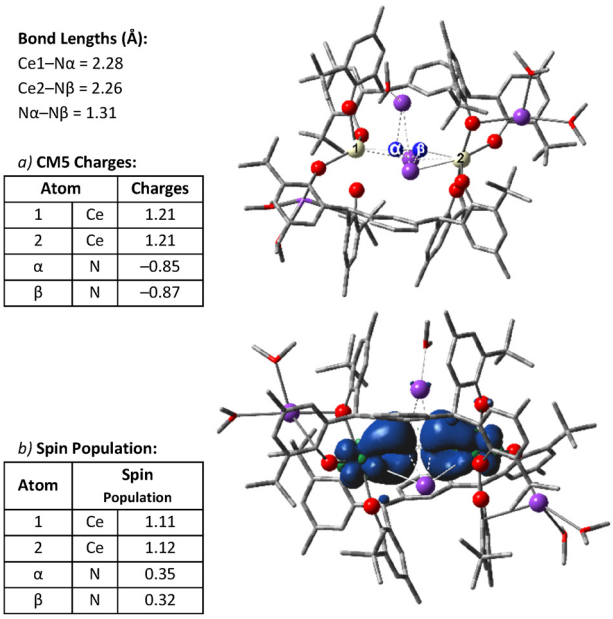


Fig. 2 Geometry of Intermediate **3** in the quartet spin state (atom colour coding: Ce = yellow, K = purple, N = blue, O = red, C = grey), optimised at the PBE0-D3BJ/BS1 level, with (a) CM5 charges and (b) spin density distribution, calculated at the PBE0-D3BJ/BS2/SMD//PBE0-D3BJ/BS1 level of theory. Isosurfaces are plotted at an isovalue of 0.0009, with blue representing excess α spin density and green representing excess β spin density. Spin populations are listed for selected atoms, consistent with partially reduced metal centres and a significantly activated, partially reduced $N_2$ unit. Nα and Nβ denote the two nitrogen atoms coordinated to $Ce_1$ and $Ce_2$, respectively. Hydrogen atoms are omitted for clarity.

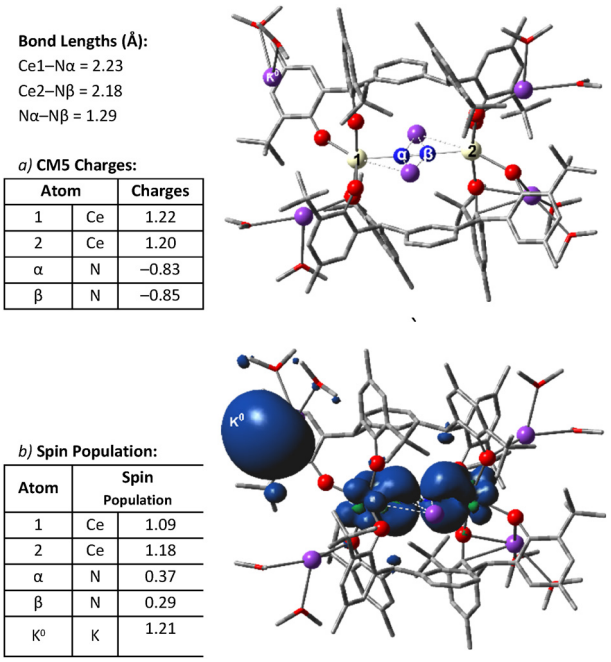


Fig. 3 Geometry of Intermediate **4** in the quintet spin state (atom colour coding: Ce = yellow, K = purple, N = blue, O = red, C = grey), optimised at the PBE0-D3BJ/BS1 level, (a) CM5 charges and (b) spin density distribution, calculated at the PBE0-D3BJ/BS2/SMD//PBE0-D3BJ/BS1 level of theory. Isosurfaces are plotted at an isovalue of 0.0009, with blue representing excess α spin density and green representing excess β spin density. The spin density is delocalised over the $\{Ce_2(\mu\text{-}\eta^1{:}\eta^1\text{-}N_2)\}$ core, while one unpaired electron remains localised on an outer $K^0$. Nα and Nβ denote the two nitrogen atoms coordinated to $Ce_1$ and $Ce_2$, respectively. Hydrogen atoms are omitted for clarity.

+1.21 e for both cerium centres and −0.87 e and −0.85 e for the two nitrogen atoms, resulting in a total $N_2$ charge of approximately −1.72 e (Fig. 2a). Spin-density analysis (Fig. 2b) reveals 1.11–1.12 unpaired electrons on the Ce atoms and 0.32 and 0.35 on the N atoms. These charge and spin density findings indicate that the cerium centres retain their $4f^1$ configurations, with the $N_2$ ligand being more reduced than in **2**.

Intermediate **4**, $[K_2K'_4(OMe_2)_8\{Ce_2(m\text{TP})_2(\mu\text{-}\eta^1{:}\eta^1\text{-}N_2)\}]$, was optimised in multiple spin states after four-electron reduction, with the quintet configuration identified as the most stable (Fig. 3). The optimised geometry exhibits Ce–N bond lengths of 2.18 and 2.23 Å and an N–N bond length of 1.29 Å. Notably, the N–N stretching frequency increases to 1390 $cm^{-1}$ in Intermediate **4**, consistent with the absence of further N–N weakening relative to Intermediate **3** and supporting the conclusion that the additional reducing equivalent is not incorporated into the $N_2$ π manifold. Two $K^+$ cations are retained within the central cavity, while four additional $K^+$ or neutral K atoms are positioned externally to simulate the full coordination environment. In this model, the externally located $K^+/K^0$ species are each coordinated by two explicit ether donors, whereas the two potassium cations residing within the *m*TP cavity are not further microsolvated because they are already stabilised by strong K–$N_2$/K–O(*m*TP) contacts and $\eta^4$ aryl interactions within a sterically saturated cavity; remaining bulk solvation is treated implicitly (SMD, THF). Spin-density analysis (Fig. 3b) reveals that only about three unpaired electrons are delocalised across the $\{Ce_2(\mu\text{-}\eta^1{:}\eta^1\text{-}N_2)\}$ core, while the fourth remains localised on an outer $K^0$ atom and is not incorporated into the framework. CM5 charge data corroborates this assignment, indicating that despite formal four-electron reduction, the electronic and structural features remain inconsistent with formation of a fully reduced $N_2^{4-}$ species. Notably, the spin density and charge of the $N_2$ unit are very similar in Intermediates **3** and **4**, consistent with the fourth electron residing on potassium rather than the core. As such, Intermediate **3** is proposed to represent the electronically and thermodynamically accessible limit of $N_2$ activation within this Ce–*m*TP system, beyond which further reduction results in localisation of electron density on external potassium centres rather than enhanced population of the $N_2$ π* manifold or additional N–N bond weakening.

## Frontier molecular orbital occupations

To further probe the electronic structure of intermediates **2**, **3**, and **4** we turned to analysis of their frontier molecular orbitals. The two electrons added during reduction to form Intermediate **2** occupy the α-spin HOMO (535α) and HOMO−1 (534α), both of which exhibit significant $N_2$ π* character (∼68% combined) with subsidiary Ce 5d/4f contributions (∼16% in the HOMO, ∼17% in the HOMO−1) (Fig. 4). In contrast, deeper orbitals such as HOMO−2 (533α) and HOMO−3 (532α) are >92%

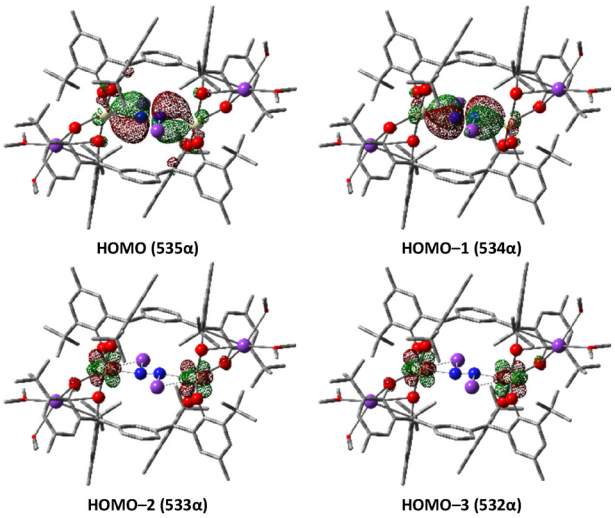


Fig. 4 Selected α-spin molecular orbitals of Intermediate **2** in the quintet spin state (atom colour coding: Ce = yellow, K = purple, N = blue, O = red, C = grey), calculated at the PBE0-D3BJ/BS2/SMD//PBE0-D3BJ/BS1 level of theory. Isosurfaces are plotted at an isovalue of 0.03. Orbital phases are represented by red (positive) and green (negative) regions.

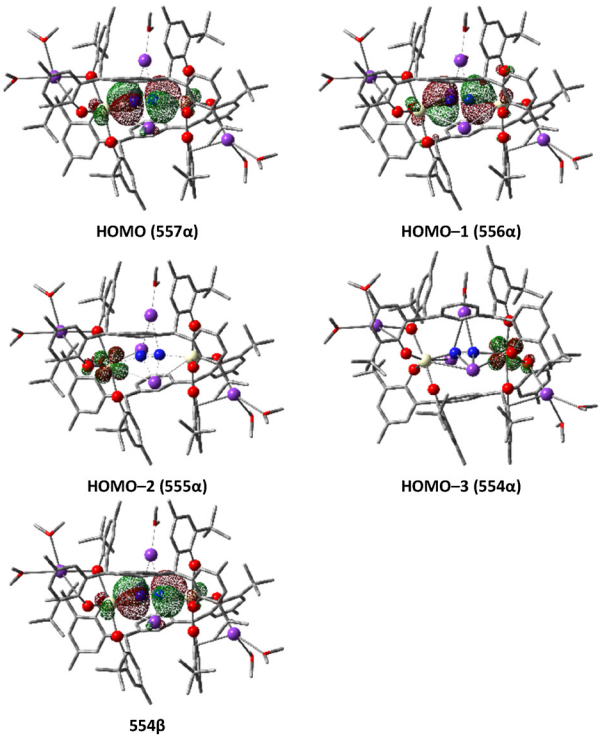


Fig. 5 Selected α- and β-spin molecular orbitals of Intermediate **3** in the quartet spin state (atom colour coding: Ce = yellow, K = purple, N = blue, O = red, C = grey), calculated at the PBE0-D3BJ/BS2/SMD//PBE0-D3BJ/BS1 level of theory. Isosurfaces are plotted at an isovalue of 0.03. Orbital phases are represented by red (positive) and green (negative) regions.

Ce-localised, confirming that the added electron density resides primarily on the $N_2$ ligand. Thus, the overall electronic structure is best described as a mixed-valent species containing partially reduced $N_2$ ligand.

By contrast to the Ti[9] and U[8] frameworks, the Ce system shows cooperative, genuinely bridging, bimetallic end-on binding upon reduction. Here, "Ti" and "U" refer to the previously reported tetraphenolate-supported Ti[9] and U[8] platforms $[Ti_2(mTP)_2]$ and $[K_2U_2(THF)_4(mTP)_2]$. We introduce them here as mechanistic comparisons to illustrate how metal–metal separation and alkali-cation assistance can control whether $N_2$ binds in a bimetallic bridging mode or at a single metal centre. In complex **1**, the Ce–Ce distance is 9.67 Å with two external solvent molecules and, after two-electron reduction, internal $N_2$ binding contracts the Ce–Ce distance to 5.98 Å (Intermediate **2**), enabling a symmetric $\mu$-$\eta^1$:$\eta^1$-$N_2$ arrangement whose frontier MOs are $N_2$ $\pi^*$-dominated with appreciable Ce 5d/4f mixing. By contrast, the Ti system maintains a larger Ti–Ti distance (7.89 Å XRD; 7.81 Å DFT) and end-on $N_2$-binding to a single Ti during catalysis (Ti–N ≈ 1.90 Å), while pulsed electron paramagnetic resonance (EPR) on **1Ti–$N_2$** shows very small $^{15}N$ hyperfine (~0.2 MHz) consistent with minimal Ti–N covalency and long Ti–N (~3–4 Å) in the isolated reduced adduct.[9] Uranium sits between these extremes: **1U** has a U–U distance of 6.57 Å, which contracts to 4.64 Å in the four-electron-reduced, U($\mu$-$\eta^2$:$\eta^2$-$N_2H_2$)U-containing product, in which $K^+$ cation inclusion was shown to be essential to stabilise charge and enable binding-mode changes during reduction.[8] These comparisons support that two-metal engagement is structurally enabled and electronically consequential in both the Ce and U systems, whereas Ti relies more on group-1-assisted, single-metal end-on chemistry.[9]

Molecular orbital analysis of the three-electron-reduced Intermediate **3** further corroborates this assignment (Fig. 5). The α-spin HOMO (orbital 557α) is of $N_2$ $\pi^*$ character (~66% combined) with additional contributions from $Ce_1$ (~14%) and $Ce_2$ (~12%). Similarly, the HOMO−1 (orbital 556α) has strong $N_2$ contributions (~68% total) alongside $Ce_1$ (~10%) and $Ce_2$ (~9%). Thus, two electrons occupy α-spin N–N $\pi^*$ orbitals. Examination of the β MO manifold finds $N_2$ $\pi^*$ orbital 554β, which is ~32% Nα and ~35% Nβ, and these three orbitals together account for the observed increase in N–N bond length, greater negative charge on $N_2$, and reduced $N_2$ spin density in Intermediate **3**—all consistent with additional $\pi^*$ occupation in the β-spin channel. In contrast, the two Ce 4f-based MOs are HOMO−2 (555α), localised almost entirely on $Ce_2$ (>96%), and HOMO−3 (554α), localised almost entirely on $Ce_1$ (~96%).

In intermediate **4**, the α-spin HOMO (orbital 606α) is almost entirely localised on an external potassium atom (~99%), consistent with the presence of a $K^0$ species and in agreement with the spin density analysis that identified one unpaired electron residing outside the {Ce($\mu$-$\eta^1$:$\eta^1$-$N_2$)Ce} core (Fig. 6). HOMO−1 (orbital 605α) and HOMO−2 (orbital 603α) both retain significant $N_2$ $\pi^*$ contributions (~27–30% from each N atom), together with appreciable mixing from the Ce centres (~13–15%). By contrast, HOMO–3 (603α) and HOMO–4 (602α) are overwhelmingly Ce-centred (>95% f-character across the two Ce atoms). The β manifold contains an orbital (602β) with $N_2$ $\pi^*$ character (~29–31% on N), consistent with occupation of a β $\pi^*$ orbital. Together, these results show that intermediate **4**

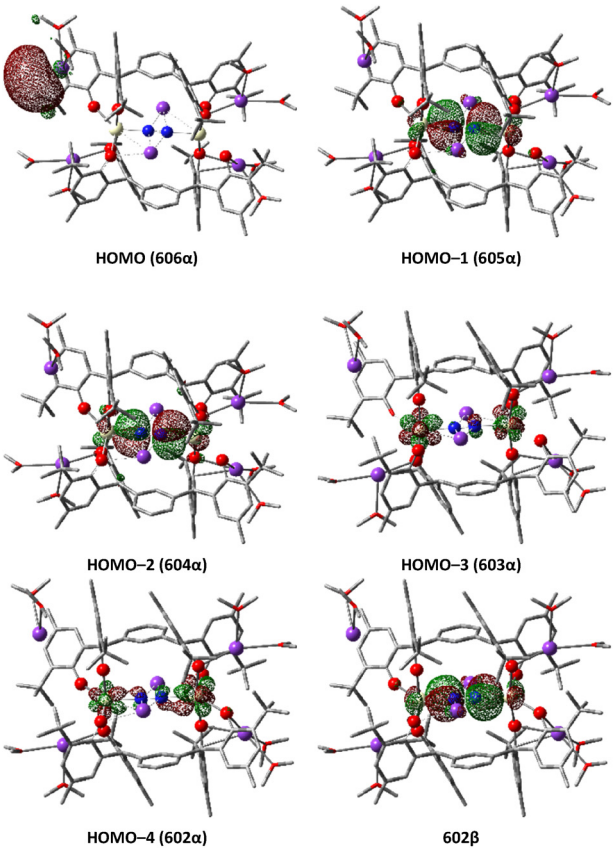


Fig. 6 Selected α-spin and β-spin molecular orbitals of Intermediate **4** in the quintet spin state (atom colour coding: Ce = yellow, K = purple, N = blue, O = red, C = grey), calculated at the PBE0-D3BJ/BS2/SMD//PBE0-D3BJ/BS1 level of theory. Isosurfaces are plotted at an isovalue of 0.03. Orbital phases are represented by red (positive) and green (negative) regions. The HOMO resides on $K^0$, confirming the fourth electron is localised externally rather than on the $N_2$ unit.

retains three electrons delocalised over the Ce–$N_2$ framework, as in intermediate **3**, while the additional (fourth) electron is instead localised on $K^0$ rather than filling the $N_2$ π* orbital.

### Dehydrometallation following three-electron reduction

A key feature of the *m*TP ligand is the benzylic H that is placed close to the Ln-bound reduced substrate, here $N_2$. In the $U_2$(*m*TP)$_2$-catalysed N2RR reactions, it was hypothesised, and supported by DFT calculations, that the first N-element bond was formed by deprotonation of one benzylic H in each *m*TP ligand by the reduced $N_2$, forming the pentaanionic ligand mentioned above *m*TP$^-$ {(OC$_6$H$_2$-2-$^t$Bu-4-Me)$_2$C}{(OC$_6$H$_2$-2-$^t$Bu-4-Me)$_2$CH}-1,3-C$_6$H$_4$. This was useful as the first N-element bond is the most challenging, and the reaction also enabled the development of the first clean catalysed routes for conversion of $N_2$ to secondary silylamines. However, we have not observed N–H bond formation in ongoing experimental studies of the reduction of **1**. While this could be due to secondary reactions with the excess K metal present, the geometry of the $Ln_2$(*m*TP)$_2$ cavity (studied in THF solvent) directs four benzylic CH groups into the cavity, in contrast to that of the $U_2$(*m*TP)$_2$ cavity (studied in arene solvent) which directs only two benzylic CH groups into the cavity.

| CM5 Charges: | | |
|---|---|---|
| Atom | | Charges |
| 1 | Ce | 1.28 |
| 2 | Ce | 1.22 |
| α | N | −0.80 |
| β | N$^H$ | −0.44 |
| C26 | C$^{benz}$ | −0.16 |
| **Spin Population:** | | |
| Atom | | Spin Population |
| 1 | Ce | 1.09 |
| 2 | Ce | 1.00 |
| α | N | 0.50 |
| β | N$^H$ | 0.50 |
| C26 | C$^{benz}$ | 0.02 |

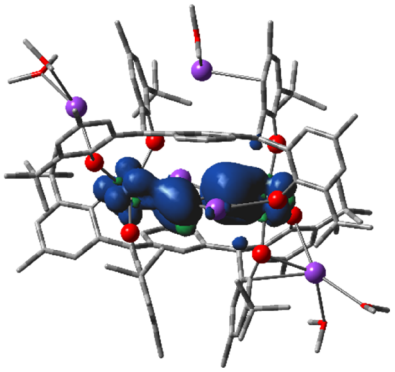

Fig. 7 Spin density distribution of Intermediate **5** in the quartet spin state (atom colour coding: Ce = yellow, K = purple, N = blue, O = red, C = grey), calculated at the PBE0-D3BJ/BS2/SMD//PBE0-D3BJ/BS1 level of theory (isovalue: 0.0009), with blue representing excess α spin density and green representing excess β spin density. Spin populations and CM5 charges are listed for selected atoms. Hydrogen atoms are omitted for clarity.

To assess whether proton abstraction from the coordinated *m*TP might facilitate $N_2$ functionalisation in the present study, a dehydrometallation step was examined from Intermediate **3**. A deprotonated species, Intermediate **5**, [K$_2$K′$_2$(OMe$_2$)$_4$K″(OMe$_2$)-{Ce$_2$(NN$^H$)(*m*TP)(*m*TP$^-$)}], in the quartet spin state, was generated by formal removal of a benzylic C–H proton. The associated Gibbs energy change was calculated as +5.1 kcal mol$^{-1}$, indicating thermodynamic accessibility, albeit with limited favourability under standard conditions.

The resulting electronic structure, however, proved incompatible with Ce–C bond formation. Spin-density analysis (Fig. 7) reveals that unpaired electron density remains localised on the Ce centres (Ce$_1$ = 1.09 e$^-$, Ce$_2$ = 1.00 e$^-$) and the $N_2$ ligand (Nα = Nβ = 0.50 e$^-$), while the deprotonated benzylic carbon (C26) carries only 0.02 e$^-$. CM5 charge analysis supports these findings, with the benzylic carbon bearing only a modest anionic character (−0.16 e$^-$). These results suggest that neither significant radical character nor appreciable negative charge has been transferred to the deprotonated carbon, both of which would be essential for stable Ce–C bond formation. Also, the calculated Ce–C26 distance of 2.70 Å in Intermediate **5**, although shorter than the 3.43 Å observed in Intermediate **3**, remains rather longer than reported Ce–C bond lengths of ∼2.44–2.58 Å,[49,50] further supporting the conclusion that no significant bonding interaction is present between Ce and the deprotonated carbon centre. The composition of the HOMO (557α, Fig. 8) supports this conclusion, showing a ∼35% contribution at C26, predominantly of p character (∼89%), with small Ce participation (∼4.6%) and minor N contributions (∼6.7%), consistent with a ligand-centred, π-delocalised orbital rather than a Ce–C bond. Furthermore, the HOMO−1 (MO 556α) is dominated by $N_2$-centred contributions (≈68%) and the HOMO−2 (MO 555α) has some Ce$_2$ (≈38%) character but with negligible carbon content (Fig. 8). The lack of any frontier orbital with simultaneous

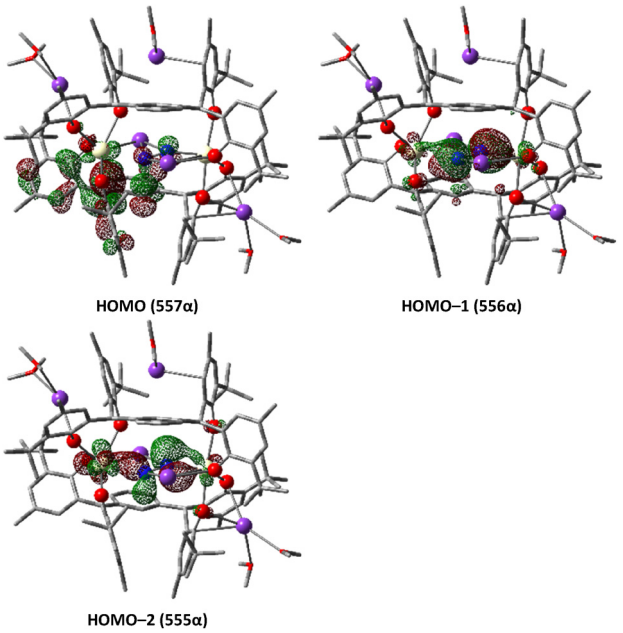


Fig. 8 Selected α-spin molecular orbitals of Intermediate **5** in the quartet spin state (atom colour coding: Ce = yellow, K = purple, N = blue, O = red, C = grey), calculated at the PBE0-D3BJ/BS2/SMD//PBE0-D3BJ/BS1 level of theory. Isosurfaces are plotted at an isovalue of 0.03. Orbital phases are represented by blue (positive) and green (negative) regions.

and appreciable contributions from both Ce and C atoms, together with the spin density distribution, indicates a lack of significant Ce–C interaction. Possible K–C interactions were examined and none were identified; all K–C separations were too long to constitute a stabilising contact.

Taken together, these data indicate that modestly endergonic dehydrometallation yields an electronically frustrated species in which the putative carbanion is neither spin- nor charge-stabilised by the metal centres. In the $U_2(m\text{TP})_2$ system, a genuinely tetraanionic $N_2^{4-}$ fragment is sufficiently basic to deprotonate the benzylic *m*TP sites and form stabilising N–H bonds,[8] but in the present Ce system the $N_2$ fragment does not reach the tetraanionic state, so there is a much weaker driving force for benzylic deprotonation and N–H bond formation. Consistent with this, our calculations show no significant Ce–C bonding to the deprotonated carbon, and the resulting carbanion remains poorly stabilised. As such, this transformation does not constitute a viable route to $N_2$ functionalisation within the Ce–*m*TP platform. Alternative pathways involving direct electron and proton transfer to the $N_2$ ligand—such as the experimentally supported concerted $K^0$/TMSCl silylation mechanism discussed below—are likely to offer more productive routes towards N–Si bond formation.

### Silylation at the two-electron reduction stage

To evaluate whether functionalisation of $N_2$ could be achieved at an earlier stage of reduction, an analysis was conducted on the two-electron reduced complex **2**. A direct silylation step using trimethylsilyl chloride (TMSCl) was modelled from this intermediate to assess the viability of N–Si bond formation.

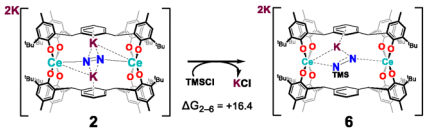


Scheme 5 Computed Gibbs energy change (in kcal $mol^{-1}$) for direct silylation of the two-electron reduced complex **2** with TMSCl, calculated at the PBE0-D3BJ/BS2/SMD//PBE0-D3BJ/BS1 level of theory.

However, the calculated Gibbs energy change for this transformation (to Intermediate **6**, $[KK'_2(OMe_2)_4\{Ce_2(m\text{TP})_2(\mu\text{-}\eta^1\text{:}\eta^1\text{-N(TMS)–N)}\}]$) was found to be +16.4 kcal $mol^{-1}$, indicating that the reaction is thermodynamically unfavourable (Scheme 5). This penalty is significantly higher than the Gibbs energy change associated with the dehydrometallation calculated above (following the three-electron reduction), which was only mildly endergonic. This lack of reactivity of the $N_2^{2-}$ agrees with our stoichiometric experimental reactions and the wide body of d-block N2RR literature that suggests that at least three-electron reduction is necessary to promote N-element bond formation with an electrophile.[24,51–54] Notably, this result demonstrates that favourable ion-pairing/halide capture alone does not render N–Si bond formation thermodynamically accessible; instead, the intrinsic electronic state of the $\{Ce_2(\mu\text{-}\eta^1\text{:}\eta^1\text{-}N_2)\}$ core is decisive.

The limited reactivity at the two-electron reduction stage highlights the electronic constraints imposed by the $\{Ce_2(\mu\text{-}\eta^1\text{:}\eta^1\text{-}N_2)\}$ architecture, which fails to sufficiently weaken the N–N bond or localise sufficient negative charge for nucleophilic attack. Taken together, these findings suggest that, following two-electron reduction, the functionalisation of $N_2$ within Ce–*m*TP complexes is unlikely to proceed efficiently without additional electron transfer. Mechanistic alternatives that couple reduction with substrate delivery—such as the concerted $K^0$/TMSCl pathway—are therefore now examined as more viable routes to N–Si bond formation.

### Mechanistic insights into $N_2$ activation and silylation

Building upon the mechanistic limitations identified at the two- and three-electron reduction levels, a full catalytic sequence was next explored, focusing on pathways that integrate electron transfer with electrophilic substrate activation. Although the catalytic sequence was initiated from Intermediate **2** rather than Intermediate **3**, functionalisation does not occur directly from this two-electron-reduced state. Instead, it becomes viable only when the third electron is delivered in concert with TMSCl uptake, through a coupled reduction–silylation step. The key transformation involving the reaction of $K^0$ and TMSCl with the $Ce_2(\mu\text{-}\eta^1\text{:}\eta^1\text{-}N_2)$ framework was modelled as a concerted N–Si bond-forming event. Here, and throughout the mechanistic analysis, "$K^0$" denotes a discrete neutral potassium atom used in the molecular DFT model (*i.e.* not an explicit band-structure treatment of bulk K metal).

Given the considerable computational demands associated with the size and complexity of the Ce–*m*TP system, the methodology was modified for this stage of the investigation.

A mixed-basis set approach (BS1′) was employed, applying the small 3-21G(d) basis to peripheral substituents while retaining a higher-level 6-31G(d,p) basis for atoms around the Ce centres and the $N_2$-binding site (see Computational methodology for full details). This adjustment significantly improved computational efficiency, enabling reliable optimisation of all relevant species within the catalytic cycle without compromising structural or energetic accuracy.

As discussed above, Intermediate **2** is a quintet species with an N–N bond length of 1.24 Å and with two $K^+$ cations positioned within the central cavity engaged in electrostatic interactions with the $N_2$ ligand. From this geometry, a concerted reduction–functionalisation step involving $K^0$ and TMSCl was modelled, resulting in the formation of Intermediate **7**, $[K_2K'_2(OMe_2)_4\{Ce_2(mTP)_2(\mu\text{-}\eta^1\text{:}\eta^1\text{-}N(TMS)\text{–}N)\}]$ (Scheme 6). This transformation was computed to be highly exergonic ($\Delta G$ = −32.6 kcal mol$^{-1}$), thus supporting the feasibility of this concerted process and establishing it as a viable mechanistic entry point for N–Si bond formation. The conversion of Intermediate **2** to the mono-silylated Intermediate **7**,[55] in the quartet spin state, was found to proceed *via* the highest-energy transition state computed ($\Delta G^{\ddagger}$ = 22.1 kcal mol$^{-1}$), thereby identifying this step as turnover-limiting. In **7**, $N_2$ polarisation appears: Nβ becomes more negative (−0.70) while N(TMS) is less negative (−0.51); this accompanies N–N elongation to 1.35 Å, a longer Ce–N(TMS) (2.54 Å), and a shorter Ce–Nβ (2.26 Å). Although the charge distribution would favour functionalisation at Nβ, the steric hindrance in the cavity disfavours TMSCl approach to Nβ. Subsequent delivery of a second equivalent of $K^0$ and TMSCl yielded the bis-silylated complex Intermediate **8**, $[K_2K'_2(OMe_2)_4\{Ce_2(mTP)_2(\kappa^1\text{-}N\text{–}N(TMS)_2)\}]$, now adopting a triplet ground state ($\Delta G$ = −9.6 kcal mol$^{-1}$). Further chemical reduction and chloride displacement converts Intermediate **8** into the doublet-state Intermediate **9**, $[K_2K'_2(Me_2O)_4\{Ce_2(mTP)_2(\kappa^1\text{-}N)\}]$ ($\Delta G$ = −113.4 kcal mol$^{-1}$), completing the formation and release of the first equivalent of the $N(SiMe_3)_3$ product along with KCl. This transformation is highly exergonic, proceeding *via* cleavage of the N–N bond and elimination of one nitrogen atom as a neutral silylamine. The remaining nitrogen fragment is retained in an anionic state (CM5 charge ≈ −1.63) and remains coordinated to one of the cerium centres. Intermediate **9** thus marks the midpoint of the catalytic cycle and serves as the platform for coordination and activation of a second equivalent of $N_2$ in the subsequent half-cycle.

Following further reduction and silylation of Intermediate **9**, Intermediate **10**, $[K_2K'_2(OMe_2)_4\{Ce_2(mTP)_2(\kappa^1\text{-}NTMS)\}]$, was generated upon addition of a fourth equivalent of $K^0$ and TMSCl. This transformation was computed to be exergonic by −69.9 kcal mol$^{-1}$. The resulting triplet-state species features a formally monoanionic nitrogen fragment bearing a TMS substituent and coordinated to a single cerium centre. The final stages of the catalytic cycle involve sequential conversion of Intermediate **10** to **11**, $[K_2K'_2(OMe_2)_4\{Ce_2(mTP)_2(\kappa^1\text{-}N(TMS)_2)\}]$, followed by regeneration of the initial species, Intermediate **2**. The transformation from **10** to **11**, corresponding to the final silylation step, is exergonic by −33.0 kcal mol$^{-1}$ and proceeds with a low activation barrier of 5.6 kcal mol$^{-1}$. In Intermediate **11**, the nitrogen fragment is doubly silylated and coordinates

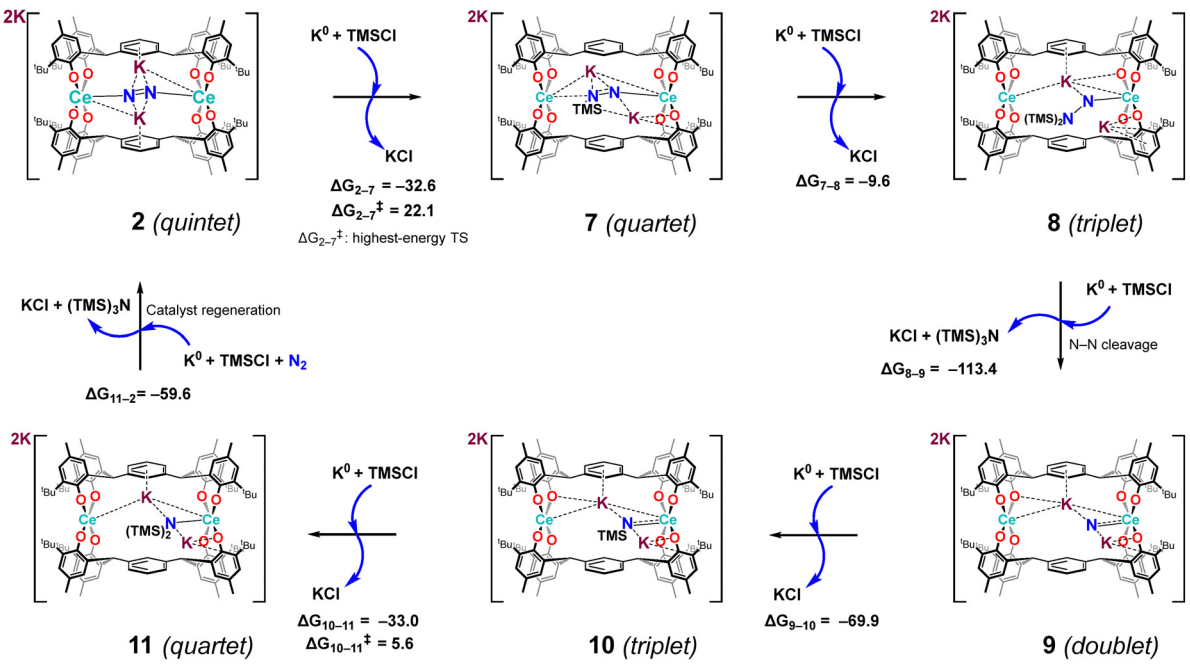


Scheme 6 Computed catalytic cycle for the reductive silylation of $N_2$ mediated by the Ce–*m*TP system, showing key intermediates (**2**, **7**–**11**) and associated Gibbs energy changes (kcal mol$^{-1}$). Calculations were performed at the PBE0-D3BJ/BS2/SMD//PBE0-D3BJ/BS1′ level of theory. The mechanism features a turnover-limiting concerted reduction–silylation step (**2** → **7**), N–N bond cleavage during the formation of Intermediate **9**, and regeneration of the active species (**2**) upon product release and $N_2$ coordination. Ground-state spin multiplicities are indicated for each intermediate in the scheme.

asymmetrically to one of the cerium centres. Release of the second equivalent of the $N(SiMe_3)_3$ product occurs upon binding of the next equivalent of $N_2$ (in the presence of $K^0$ reductant), thereby regenerating Intermediate **2** with an associated Gibbs energy change of $-59.6$ kcal mol$^{-1}$. These results demonstrate the thermodynamic feasibility of completing the full catalytic cycle under mild conditions.

## Summary and conclusions

A detailed theoretical investigation has been conducted to elucidate the mechanisms and thermodynamic feasibility of $N_2$ activation and functionalisation within a bimetallic Ce–*m*TP metallacyclic framework. DFT calculations, incorporating dispersion corrections and the SMD continuum solvation model, were applied to systematically evaluate multi-electron reduction steps, the influence of $K^+$ cations, and the role of $K^0$ as a chemical reductant. Potential reaction pathways for N–Si bond formation were also explored, including both direct and concerted silylation events. The results collectively establish the electronic limits of $N_2$ activation and demonstrate that functionalisation is viable only when electron transfer and substrate delivery are tightly coupled within this f-block system.

Initial reduction studies indicated that, in the absence of $K^+$, even a two-electron reduction of the bridging $N_2$ ligand is electronically constrained and thermodynamically disfavoured. Upon incorporation of two $K^+$ cations within the central cavity, the first two-electron reduction is rendered strongly exergonic ($\Delta G = -125.7$ kcal mol$^{-1}$), underscoring the stabilising influence of alkali metal coordination. A formal four-electron reduction was subsequently computed; however, the associated reduction potential of $-4.48$ V is prohibitively negative for application with conventional reductants.

We then turned to the evaluation of $K^0$ as a chemical reductant. Detailed CM5 charge, spin density and molecular orbital composition analyses were undertaken to assess the localisation of the added electron density. These investigations revealed that full localisation of four electrons on the $N_2$ moiety was not achieved. Rather, the third electron was found to be partially delocalised across the $N_2$ $\pi^*$ orbitals and the cerium centres, while the fourth electron remained largely localised on an external potassium atom, with negligible participation in the metal–ligand bonding framework. The three-electron-reduced species (Intermediate **3**) exhibits an N–N bond length of 1.31 Å and a total charge of approximately $-1.7$ e on the $N_2$ fragment, consistent with partial reduction and activation of the $N_2$ ligand. In contrast, the four-electron-reduced structure did not display further elongation of the N–N bond or increased $\pi^*$ occupation. Collectively, these findings establish Intermediate **3** as the electronic and thermodynamic upper limit of $N_2$ activation achievable within the Ce–*m*TP framework. Beyond this point, further electron addition does not lead to formation of a genuine $N_2^{4-}$ species.

Alternative activation strategies were also explored. A dehydrometallation pathway, involving benzylic proton abstraction from the ligand framework, was calculated to be only mildly endergonic. However, the resulting intermediate does not exhibit meaningful Ce–C interaction or charge localisation at the deprotonated site, precluding stable bond formation. In parallel, attempts to directly silylate the reduced $N_2$ unit at the two-electron stage were found to be thermodynamically inaccessible, with a significant Gibbs energy penalty. These results highlight that additional electron transfer is necessary to sufficiently activate the $N_2$ moiety for functionalisation. Collectively, these findings underscore the requirement for concerted reductant and electrophile delivery—such as through $K^0$/TMSCl pairs—to achieve N–Si bond formation within the Ce–*m*TP platform.

To this end, a complete catalytic cycle was then modelled, in which the concerted addition of $K^0$ and TMSCl enabled successive silylation events on the partially reduced $N_2$ ligand. The proposed mechanism proceeds through six well-defined intermediates (**2**, **7**–**11**), encompassing the delivery of six electrons and six equivalents of TMSCl. Key steps include a turnover-limiting first silylation ($\Delta G^{\ddagger} = 22.1$ kcal mol$^{-1}$), formation of mono- and bis-silylated species, and cleavage of the N–N bond after the third electron transfer, releasing the first equivalent of $N(SiMe_3)_3$. The remaining nitrogen fragment, retained in a monoanionic state, is further reduced and silylated in the second half-cycle, culminating in regeneration of Intermediate **2** upon re-coordination of $N_2$. The overall process is highly exergonic, and all computed barriers—including the final N–Si bond formation ($\Delta G^{\ddagger} = 5.6$ kcal mol$^{-1}$)—are consistent with feasibility under experimentally relevant conditions.

Collectively, these results provide a detailed mechanistic framework for understanding $N_2$ activation and functionalisation in Ce–*m*TP complexes, highlighting the critical roles played by alkali metal coordination, stepwise electron delivery, and concerted reductant–electrophile addition in modulating $N_2$ reactivity. This work therefore lays a robust theoretical foundation for the rational design of rare-earth-based catalysts capable of promoting multi-electron small-molecule activation and functionalisation under mild conditions.

## Computational methodology

All calculations were performed using the Gaussian 16 software package.[56] Geometry optimisations were carried out using the PBE0[57] hybrid functional with Grimme's D3 dispersion correction and Becke–Johnson damping (PBE0-D3BJ).[58] Two basis set protocols were employed. For systems studied prior to the mechanistic investigation, optimisations were performed using the BS1 basis set, which comprised the Stuttgart RSC ECP[59] and associated segmented valence basis set for cerium, and the 6-31G(d,p)[60,61] basis set for all other atoms. To reduce computational cost while preserving key coordination features, dimethyl ether—chosen for its electronic resemblance to THF—was used as the explicit solvent in place of THF. Potassium species located outside the $Ce_2(mTP)_2$ cavity were modelled with two explicit ether donors per K to represent first-shell microsolvation,

whereas potassium ions residing within the cavity were not solvated by explicit ether molecules because the cavity is sterically saturated and the $K^+$ ions are already engaged in close contacts to $N_2$/aryl/phenolate donors; longer-range solvation is captured by the implicit SMD(THF) treatment. In steps where potassium metal is invoked as the reductant (*e.g.* Scheme 4 and the catalytic cycle), each reducing equivalent is represented as a single neutral potassium atom ("$K^0$") within this molecular framework, *i.e.* not a periodic (band-structure) treatment of bulk potassium metal.

For all species relevant to the reaction mechanism, geometry optimisations were performed using a modified mixed-basis scheme, denoted BS1′. At this level, cerium, potassium and the non-metal atoms involved in the chemically active region (*i.e.* coordinating ligands and solvent molecules) were treated as previously, whereas peripheral atoms of bulky substituents were described using the more compact 3-21G(d) basis set. This mixed-basis approach offered significant computational efficiency without compromising accuracy. Its reliability was confirmed by benchmarking geometries and free energies against BS1-level calculations, which yielded excellent agreement (see Section S4 of the SI).

Vibrational frequency calculations were performed to characterise all stationary points. Minima were confirmed by the absence of imaginary frequencies, while transition states were identified by a single imaginary frequency corresponding to the expected reaction coordinate. These calculations also yielded zero-point vibrational energies and thermal corrections to furnish the Gibbs energy at 298.15 K and 1 atm, based on the ideal-gas, rigid-rotator, harmonic oscillator approximation. To avoid overestimation of entropy from low-frequency modes, all real frequencies below 100 $cm^{-1}$ were replaced by 100 $cm^{-1}$ following the Truhlar-type cut-off protocol.[62,63]

Single-point energies were computed at the PBE0-D3BJ[57,58] level using the SMD implicit solvation model with THF as the solvent. These calculations employed the BS2 basis set, which included Stuttgart RSC ECP[59] and associated segmented valence basis set for cerium, and the 6-311+G(d,p)[64,65] basis set for potassium and all non-metal atoms. Solution-phase Gibbs energies were obtained by combining the solvent-phase electronic energies with gas-phase thermal corrections derived from BS1 or BS1′ frequency calculations.

Reduction potentials were calculated for the general redox process:

$$O_{(soln)} + ne^-_{(g)} \rightarrow R_{(soln)}$$

using the equation:

$$E^\circ_{O/R} = -\frac{\Delta G^\circ_{O/R}}{nF} - E^\circ_{abs}(Fc/Fc^+),$$

where $\Delta G^\circ_{O/R}$ is the Gibbs energy change, $n$ is the number of electrons transferred and $F$ is the Faraday constant. The absolute potential of the ferrocene/ferrocenium couple, $E^\circ_{abs}(Fc/Fc^+) = 5.08\,V$,[66,67] was used to shift the vacuum-referenced potential to the $Fc/Fc^+$ scale.

## Author contributions

Conceptualization: SA, NK, PLA. Investigation: SA. Formal Analysis: SA, NK. Draft Writing: SA, NK. Funding acquisition: NK, PLA. Resources: NK. Supervision: NK, PLA. Reviewing and editing: all authors.

## Conflicts of interest

There are no conflicts to declare.

## Data availability

The data supporting this article have been uploaded as part of the supplementary information (SI). The supplementary information contains additional computational details and analyses, including orbital/spin-density and charge analyses, benchmarking of optimisation protocols, and XYZ coordinates with SCF energies for key Ce–mTP/N2 intermediates and transition states. See DOI: https://doi.org/10.1039/d6cp00343e.

## Acknowledgements

We are grateful to the EPSRC for funding this project (EP/X042049/1). We also thank the University of Manchester for access to its Computational Shared Facility and associated support services. Conceptualization of the different components of the underpinning experimental studies, and writing of the manuscript (PLA) were supported by the National Science Foundation (cation studies NSF, CHE-2154369), the Catalysis Program in the U.S. Department of Energy Office of Science, Office of Basic Energy Sciences, Chemical Sciences, Geosciences, and Biosciences Division, at the Lawrence Berkeley National Laboratory under contract no. DE-AC02-05CH11231 (lanthanide catalyses), and the European Research Council (ERC) under the European Union's Horizon 2020 research and innovation programme, grant agreement No 740311 (reaction design and early mechanistic components). We are also grateful to Dr Anthony Wong, Mr Matthew Hernandez and Mr Jaden Lara for helpful discussions.

## Notes and references

1 J. W. Erisman, M. A. Sutton, J. Galloway, Z. Klimont and W. Winiwarter, *Nat. Geosci.*, 2008, **1**, 636–639.
2 Y. Tanaka, M. Ogawa and A. S. Jursa, *J. Chem. Phys.*, 1964, **40**, 3690–3700.
3 X. Tang, Y. Hou, C. Y. Ng and B. Ruscic, *J. Chem. Phys.*, 2005, **123**, 74330.
4 F. R. Gilmore, *J. Quant. Spectrosc. Radiat. Transfer.*, 1965, **5**, 369-IN3.
5 J. Nørskov, J. Chen, R. Miranda, T. Fitzsimmons and R. Stack, *Sustainable Ammonia Synthesis – Exploring the scientific challenges associated with discovering alternative, sustainable processes for ammonia production*, United States Department of Energy, 2016.

6 M. H. Hasan, T. M. Mahlia, M. Mofijur, I. M. Rizwanul Fattah, F. Handayani, H. C. Ong and A. S. Silitonga, *Energies*, 2021, 14.
7 C. Smith, A. K. Hill and L. Torrente-Murciano, *Energy Environ. Sci.*, 2020, **13**, 331–344.
8 P. L. Arnold, T. Ochiai, F. Y. T. Lam, R. P. Kelly, M. L. Seymour and L. Maron, *Nat. Chem.*, 2020, **12**, 654–659.
9 A. Wong, F. Y. T. Lam, M. Hernandez, J. Lara, T. M. Trinh, R. P. Kelly, T. Ochiai, G. Rao, R. D. Britt, N. Kaltsoyannis and P. L. Arnold, *Chem. Catal.*, 2024, 100964.
10 M. J. Chalkley, T. J. Del Castillo, B. D. Matson and J. C. Peters, *J. Am. Chem. Soc.*, 2018, **140**, 6122–6129.
11 K. Arashiba, Y. Miyake and Y. Nishibayashi, *Nat. Chem.*, 2011, **3**, 120–125.
12 J. S. Anderson, J. Rittle and J. C. Peters, *Nature*, 2013, **501**, 84–87.
13 S. Kuriyama, K. Arashiba, K. Nakajima, Y. Matsuo, H. Tanaka, K. Ishii, K. Yoshizawa and Y. Nishibayashi, *Nat. Commun.*, 2016, **7**, 12181.
14 S. J. K. Forrest, B. Schluschaß, E. Y. Yuzik-Klimova and S. Schneider, *Chem. Rev.*, 2021, **121**, 6522–6587.
15 F. Masero, M. A. Perrin, S. Dey and V. Mougel, *Chem. – Eur. J.*, 2021, **27**, 3892–3928.
16 S. Kim, F. Loose and P. J. Chirik, *Chem. Rev.*, 2020, **120**, 5637–5681.
17 Y. Tanabe and Y. Nishibayashi, *Coord. Chem. Rev.*, 2022, **472**, 214783.
18 C. H. Beasley, O. L. Duletski, K. S. Stankevich, N. Arulsamy and M. T. Mock, *Dalton Trans.*, 2024, **53**, 6496–6500.
19 J. C. Peters, *Faraday Discuss.*, 2023, **243**, 450–472.
20 S.-L. Meng, X.-B. Li, C.-H. Tung and L.-Z. Wu, *Chem*, 2021, **7**, 1431–1450.
21 Z.-J. Lv, J. Wei, W.-X. Zhang, P. Chen, D. Deng, Z.-J. Shi and Z. Xi, *Natl. Sci. Rev.*, 2020, **7**, 1564–1583.
22 B. M. Lindley, R. S. van Alten, M. Finger, F. Schendzielorz, C. Würtele, A. J. M. Miller, I. Siewert and S. Schneider, *J. Am. Chem. Soc.*, 2018, **140**, 7922–7935.
23 Y. Roux, C. Duboc and M. Gennari, *ChemPhysChem*, 2017, **18**, 2606–2617.
24 G.-X. Wang, Z.-B. Yin, J. Wei and Z. Xi, *Acc. Chem. Res.*, 2023, **56**, 3211–3222.
25 M. J. Chalkley, M. W. Drover and J. C. Peters, *Chem. Rev.*, 2020, **120**, 5582–5636.
26 P. L. Arnold, D. Patel, C. Wilson and J. B. Love, *Nature*, 2008, **451**, 315–317.
27 W. J. Evans, T. A. Ulibarri and J. W. Ziller, *J. Am. Chem. Soc.*, 1988, **110**, 6877–6879.
28 Y.-M. So and W.-H. Leung, *Coord. Chem. Rev.*, 2017, **340**, 172–197.
29 R. R. Schrock, *Acc. Chem. Res.*, 2005, **38**, 955–962.
30 R. A. Kinney, R. L. McNaughton, J. M. Chin, R. R. Schrock and B. M. Hoffman, *Inorg. Chem.*, 2011, **50**, 418–420.
31 J. S. Anderson, G. E. I. I. I. Cutsail, J. Rittle, B. A. Connor, W. A. Gunderson, L. Zhang, B. M. Hoffman and J. C. Peters, *J. Am. Chem. Soc.*, 2015, **137**, 7803–7809.
32 H. Tsurugi and K. Mashima, *J. Am. Chem. Soc.*, 2021, **143**, 7879–7890.
33 C. A. Buchanan, D. Herrera, M. Balasubramanian, B. R. Goldsmith and N. Singh, *JACS Au*, 2022, **2**, 2742–2757.
34 A. Mondal, C. G. T. Price, J. Tang and R. A. Layfield, *J. Am. Chem. Soc.*, 2023, **145**, 20121–20131.
35 J. A. Branson, P. W. Smith, D.-C. Sergentu, D. R. Russo, H. Gupta, C. H. Booth, J. Arnold, E. J. Schelter, J. Autschbach and S. G. Minasian, *J. Am. Chem. Soc.*, 2024, **146**, 25640–25655.
36 Z. Chen and J. Yang, *J. Chem. Phys.*, 2022, **156**, 211101.
37 L. A. Solola, A. V. Zabula, W. L. Dorfner, B. C. Manor, P. J. Carroll and E. J. Schelter, *J. Am. Chem. Soc.*, 2017, **139**, 2435–2442.
38 N. Mahieu, J. Piątkowski, T. Simler and G. Nocton, *Chem. Sci.*, 2023, **14**, 443–457.
39 K. C. MacLeod and P. L. Holland, *Nat. Chem.*, 2013, **5**, 559–565.
40 G. P. Connor and P. L. Holland, *Catal. Today*, 2017, **286**, 21–40.
41 M. Falcone, L. Barluzzi, J. Andrez, F. Fadaei Tirani, I. Zivkovic, A. Fabrizio, C. Corminboeuf, K. Severin and M. Mazzanti, *Nat. Chem.*, 2019, **11**, 154–160.
42 D. Singh, W. R. Buratto, J. F. Torres and L. J. Murray, *Chem. Rev.*, 2020, **120**, 5517–5581.
43 K. Grubel, W. W. Brennessel, B. Q. Mercado and P. L. Holland, *J. Am. Chem. Soc.*, 2014, **136**, 16807–16816.
44 K. Ding, A. W. Pierpont, W. W. Brennessel, G. Lukat-Rodgers, K. R. Rodgers, T. R. Cundari, E. Bill and P. L. Holland, *J. Am. Chem. Soc.*, 2009, **131**, 9471–9472.
45 N. Jori, T. Rajeshkumar, R. Scopelliti, I. Ivković, A. Sienkiewicz, L. Maron and M. Mazzanti, *Chem. Sci.*, 2022, **13**, 9232–9242.
46 A. V. Marenich, S. V. Jerome, C. J. Cramer and D. G. Truhlar, *J. Chem. Theory Comput.*, 2012, **8**, 527–541.
47 R. S. Mulliken, *J. Chem. Phys.*, 1955, **23**, 1833–1840.
48 P. Löwdin, *J. Chem. Phys.*, 1950, **18**, 365–375.
49 M. Gregson, E. Lu, F. Tuna, E. J. L. McInnes, C. Hennig, A. C. Scheinost, J. McMaster, W. Lewis, A. J. Blake, A. Kerridge and S. T. Liddle, *Chem. Sci.*, 2016, **7**, 3286–3297.
50 G. B. Panetti, D.-C. Sergentu, M. R. Gau, P. J. Carroll, J. Autschbach, P. J. Walsh and E. J. Schelter, *Nat. Commun.*, 2021, **12**, 1713.
51 A. D. Piascik, R. Li, H. J. Wilkinson, J. C. Green and A. E. Ashley, *J. Am. Chem. Soc.*, 2018, **140**, 10691–10694.
52 S. F. McWilliams, E. Bill, G. Lukat-Rodgers, K. R. Rodgers, B. Q. Mercado and P. L. Holland, *J. Am. Chem. Soc.*, 2018, **140**, 8586–8598.
53 Y. Tanabe and Y. Nishibayashi, *Coord. Chem. Rev.*, 2019, **389**, 73–93.
54 Z.-B. Yin, G.-X. Wang, X. Yan, J. Wei and Z. Xi, *Nat. Commun.*, 2025, **16**, 674.
55 We also assessed the alternative **3** + K/TMSCl → **7** transformation. Calculations indicate it is exergonic, but a full transition-state search was not pursued because

intermediate **3** is already tightly associated with three $K^+$ ions. We therefore focus on the concerted **2** → **7** pathway.

56 M. J. Frisch, G. W. Trucks, H. B. Schlegel, G. E. Scuseria, M. A. Robb, J. R. Cheeseman, G. Scalmani, V. Barone, G. A. Petersson, H. Nakatsuji, H. Li, M. Caricato, X. Li, E. V. Styris, J. V. Ortiz, K. Raghavachari, J. B. Foresman, J. Cui, Z. Li, M. Irle, S. Kim, M. S. Gordon, J. J. Dannenberg, S. Ehara, O. Mo, J. L. Fox, A. W. Lange, R. A. Yu, L. Qin, A. D. Korambath, J. E. Peralta, A. F. Izmaylov, K. Wiberg, F. Stratmann, T. Vreven, H. P. Hratchian, M. Al-Laham, A. E. Proynov, A. Allouche, M. Alam, C. Lee and J. M. Millam, *Gaussian 16, Revision C.01*, Gaussian, Inc., Wallingford CT, 2019.

57 C. Adamo and V. Barone, *J. Chem. Phys.*, 1999, **110**, 6158–6170.

58 S. Grimme, S. Ehrlich and L. Goerigk, *J. Comput. Chem.*, 2011, **32**, 1456–1465.

59 M. Dolg, H. Stoll and H. Preuss, *J. Chem. Phys.*, 1989, **90**, 1730–1734.

60 P. C. Hariharan and J. A. Pople, *Theor. Chim. Acta*, 1973, **28**, 213–222.

61 W. J. Hehre, K. Ditchfield and J. A. Pople, *J. Chem. Phys.*, 1972, **56**, 2257–2261.

62 C. J. Cramer and D. G. Truhlar, *Chem. Rev.*, 1999, **99**, 2161–2200.

63 R. F. Ribeiro, A. V. Marenich, C. J. Cramer and D. G. Truhlar, *J. Phys. Chem. B*, 2011, **115**, 14556–14562.

64 R. Krishnan, J. S. Binkley, R. Seeger and J. A. Pople, *J. Chem. Phys.*, 1980, **72**, 650–654.

65 T. Clark, J. Chandrasekhar, G. W. Spitznagel and P. V. R. Schleyer, *J. Comput. Chem.*, 1983, **4**, 294–301.

66 D. Jeon, K. C. Cho and Y. K. Kang, *Bull. Korean Chem. Soc.*, 2025, **46**, 281–292.

67 M. Namazian, C. Y. Lin and M. L. Coote, *J. Chem. Theory Comput.*, 2010, **6**, 2721–2725.

 